# The effect of ionization on cluster formation in laser ablation plumes

**M S Tillack, D W Blair and S S Harilal**

Mechanical and Aerospace Engineering Department, University of California, San Diego, 9500 Gilman Drive, La Jolla, CA 92093-0438, USA

E-mail: mtillack@ucsd.edu

**Abstract**
Ablation plumes caused by short-pulse laser irradiation provide conditions which are well suited to the formation of nanoclusters. The high saturation ratios and presence of ionization lead to extraordinarily high nucleation rates and small critical radii. We have explored the homogeneous nucleation and heterogeneous growth of condensates from Si targets expanding into a low-pressure He ambient using a Nd:YAG laser with a pulse length of 8 ns, wavelength of 532 nm and intensities in the range of $5 \times 10^7$–$5 \times 10^9$ W cm$^{-2}$. Clusters in the range of 5–50 nm have been produced. In the highly dynamic, non-linear regime of short-pulse laser–matter interactions, plume evolution and condensation processes are strongly coupled and difficult to predict accurately from modelling alone. Both numerical predictions and experimental results were used to quantify the competing effects of ionization and supersaturation. The results suggest a dominant influence of ionization for nearly all intensities above the ablation threshold.

## 1. Introduction

The interaction of laser ablation plumes with a background gas has received increased attention recently due to its importance in pulsed laser deposition [1], nanoparticle formation and growth [2–4] and laser micromachining [5]. Compared with expansion into a vacuum, the interaction of the plume with an ambient gas is a far more complex gas dynamic process due to the appearance of new physical processes such as deceleration, thermalization of the ablated species, interpenetration, recombination, formation of shock waves and clustering [6–11].

Short-pulse laser irradiation of surfaces initiates a complex sequence of events which occur both during and after the laser pulse. As depicted in figure 1, this includes laser absorption in the surface, phase change and mass expulsion in both liquid and vapour states, plasma formation leading to partial absorption in the plume, acceleration of the vapour to hypersonic velocities followed by rapid condensation and finally, in cases with sufficiently high ambient pressure, collapse of the plume remnants onto the surface. During the expansion stage, the plume front can achieve very high velocities. For example, the expansion velocity obtained with a laser intensity of $10^9$ W cm$^{-2}$ can easily reach $10^7$ cm s$^{-1}$, corresponding to a directed kinetic energy greater than 1 keV [12–14].

Expansion of the saturated vapour, combined with heat transfer at the contact surface between the plume and the ambient gas, leads to very rapid cooling. This cooling can occur more rapidly than condensation, leading to exceptionally high saturation ratios $S$, where $S$ represents the ratio of the actual vapour pressure to the saturation pressure at a given temperature: $S = p_v/p_s$.

According to classical condensation theory, the rate of homogeneous nucleation of a condensate is strongly dependent on the saturation ratio obtained. The free energy of formation of a condensate is determined from a balance between bulk cohesive forces between liquid atoms and an energy barrier due to surface tension. In terms of the cluster radius $r$, the free energy to form a spherical condensed cluster can be written as [15–17]

$$W(r) = -\tfrac{4}{3}\pi r^3 (n\Delta\mu) + 4\pi r^2 \sigma \qquad (1)$$

where $\Delta\mu = kT \ln S$ is the difference in chemical potential between the condensed and uncondensed atoms, $\sigma$ is the surface tension ($\sim$0.73 N m$^{-1}$ for Si) and $n$ is the atom
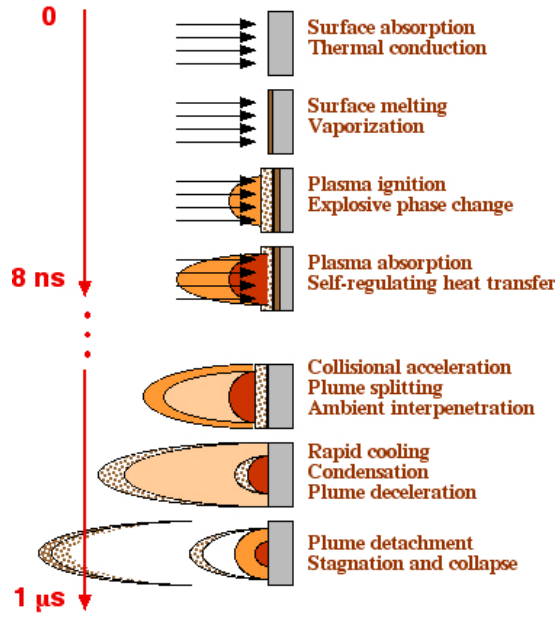
**Figure 1.** Stages of laser ablation plume creation, expansion and condensation.

(This figure is in colour only in the electronic version)



**Figure 2.** Free energy of cluster formation for Si at 2000 K and $n = 10^{20}$ cm$^{-3}$ compared with the same conditions with $Z_{\text{eff}} = 0.01$.
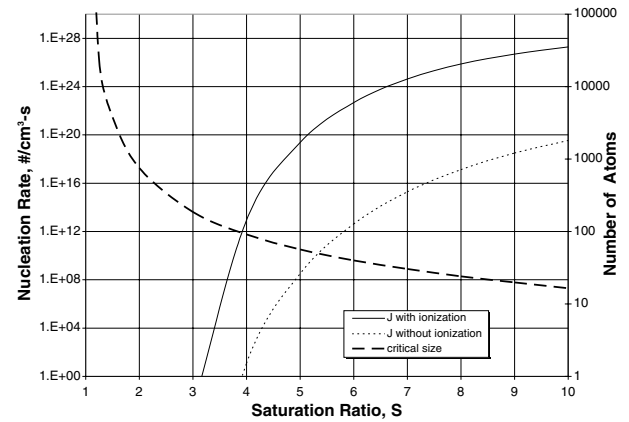


**Figure 3.** Homogeneous nucleation rate both with and without ionization for the same parameters as figure 2. Also included is the critical cluster size, which is nearly identical in this case either with or without ionization.

number density. Figure 2 shows an example of the Gibbs free energy versus the spherical cluster radius for Si at 2000 K and $n = 10^{20}$ cm$^{-3}$. The critical radius $r^*$, beyond which growth becomes energetically preferred, occurs at the maximum of $W(r)$:

$$r^* = \frac{2\sigma}{n\Delta\mu}. \qquad (2)$$

The rate of homogeneous nucleation ($J_{\text{h}}$) is proportional to the concentration of critical clusters ($C^*$), the monomer attachment frequency ($\beta$) and the Zel'dovich prefactor ($Z$) which accounts for the statistical probability that an impingement will push a critical cluster over the barrier:

$$J_{\text{h}} = Z\beta C^* \qquad (3)$$
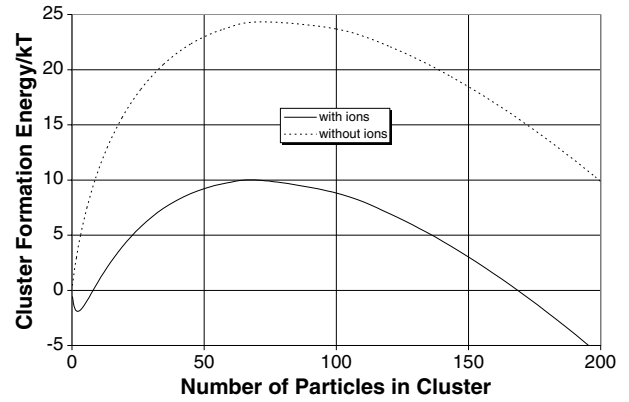
where $Z$ is given by

$$Z = \sqrt{\Delta W_k / 3\pi kT N_k^2}, \qquad (4)$$

$\Delta W_k$ is the nucleation work, i.e. the size of the barrier, and $N_k$ is the number of atoms in a critical cluster. The concentration of critical clusters is also related to the size of the barrier and is given by [18]

$$C^* = \frac{p_{\text{v}}}{kT} \exp\left(-\frac{\Delta W_k}{kT}\right). \qquad (5)$$

Figure 3 shows the resulting homogeneous nucleation rate. For the parameters in figure 2, the barrier in the absence of ionization is approximately $25kT$.

It is well known that charged ions tend to be jacketed by surrounding neutral atoms [16, 18]. If the medium consists of a dielectric material, then the electric field surrounding the ions causes polarization of the dielectric material. The polarized vapour atoms are attracted to the ion. As a result, a local minimum energy state exists, corresponding to this jacketed

ion, and the critical radius shifts to a smaller value. In addition, the energy barrier is lowered, leading to a higher homogeneous nucleation rate at any given temperature. The free energy is modified in the presence of ionization to account for this dielectric source of energy:

$$\begin{aligned} W(r) = &-\tfrac{4}{3}\pi r^3(n\Delta\mu) \\ &+ 4\pi r^2\sigma + (1 - 1/\varepsilon_{\text{c}})(Q^2/8\pi\varepsilon_o)(1/r - 1/r_a) \end{aligned} \qquad (6)$$

where $\varepsilon_{\text{c}}$ is the dielectric constant of the clusters, $Q$ is the ionic charge, $r_a$ is the radius of a jacketed ion and we assume $\varepsilon = 1$ for the vapour phase. (For Si clusters, the dielectric constant $\varepsilon_{\text{c}}$ is $\sim$12.) The critical radius is obtained by differentiating equation (6) and the nucleation rate is obtained by substituting this modified $W$ into equations (3)–(5).

These effects are depicted in figures 2 and 3, which are based on the same conditions described above, but with 1% ionization ($Z_{\text{eff}} = 0.01$). Note that ionization reduces the energy barrier substantially, leading to much higher nucleation rates owing to the exponential dependence on $\Delta W/kT$.

At sufficiently high saturation ratios, the heterogeneous nucleation on ions can become 'barrierless', such that the rate is determined only by the concentration of seed sites. In this regime, if the saturation ratio continues to increase, the homogeneous nucleation rate eventually will overtake the

ion seed pathway [16]. An understanding of this competition between ion-induced nucleation and homogeneous nucleation at high saturation ratio is not firmly established, especially within the context of laser ablation plumes.

In this work we have studied the mechanisms of cluster formation in laser plasma. Previous measurements of laser plasma have shown that non-equilibrium ionization may exist throughout the duration of cluster formation and growth [19, 20]. A mechanism for the role of ions in condensation has been proposed by previous investigators [18]. However, this model has not been applied to short-pulse laser plasma and cannot be applied properly without verifying that the assumptions behind it are valid. Numerical simulations have also been used to model the laser plasma flow [21–25]; however, none has investigated the role of ions in the condensation of the laser plasma.

We explored regimes of laser intensities from $5 \times 10^7$ to $5 \times 10^9$ W cm$^{-2}$ which provide an average charge state between 0.001 and 1 (fully ionized Si would be 14). The background gas is an important contributor to the processes of expansion and condensation, but was not studied extensively; for all cases considered here, we used He at 500 mTorr.

We have found that the amount of ionization required to provide an important influence on the condensation physics (as compared with classical supersaturation-driven condensation) is very low and can be reached with laser intensities very near the ablation threshold. We conclude that the ion seed pathway is an important consideration for nearly all laser ablation plumes.

Laser ablation plumes are highly dynamic, non-linear and provide strong coupling between the basic expansion dynamics and the processes involved in condensation. In order to provide a qualitative understanding of the time evolution of condensation within an ablation plume, a one-dimensional model of laser ablation plume behaviour was developed. Key features of the model are summarized in section 2 and example results are shown in section 3. Experiments were performed in order to directly measure the final size distribution of clusters and to provide data for a better understanding of the underlying physics. Four primary types of measurements were made:

(1) plume expansion dynamics,
(2) plasma temperature and density, which are then used to estimate saturation ratio and ionization state,
(3) spectroscopic emission from Si$_2$ dimers and its correlation with Si$^+$ ions, and
(4) final cluster size distribution.

Further details on experimental results are provided in section 4. Finally, section 5 provides a summary and conclusions derived from these experimental and modelling studies.

## 2. Model description

One of the unique aspects of condensation in laser ablation plumes is the highly dynamic nature of the plume state variables, upon which the condensation depends strongly and nonlinearly. Changes occur over many orders of magnitude during the event and across the spatial domain. In order to provide a qualitative understanding of the evolving plume state

variables and to help guide and interpret experimental studies, a numerical model of laser ablation plume behaviour was developed. The model includes all of the basic mechanisms that govern the expansion of the vapour and the subsequent condensation. Simplifications are made in several areas where the impact is believed to be small, in order provide a relatively robust scoping tool focused on only the key physics. The fluid equations are one-dimensional in the direction of the plume expansion. The model treats the various steps in the expansion summarized in section 1, including laser absorption, surface thermal response, mass evolution, plasma ionization and recombination, gas-phase hydrodynamics and heat transfer, and aerosol generation and growth. Mechanisms for aerosol ejection directly from the surface have not been treated in this work.

### Absorption in the surface

Laser absorption is modelled with a surface attenuation coefficient [5]. A fraction of the incident energy flux, $I_{in}$, is reflected and the remainder, $I_o$, is deposited volumetrically according to the Lambert–Beer law:

$$I(z) = I_o \alpha e^{-\alpha z}. \tag{7}$$

### Thermal response of the surface

The thermal response of the surface includes both heat capacity and phase change energies. The governing energy equation in the solid and liquid phases is given by

$$\frac{\partial}{\partial z}\left(\lambda_t \frac{\partial T(z,t)}{\partial z}\right) + I_o(t)\alpha e^{-\alpha z} = \frac{\partial}{\partial t}(\rho C_p T(z,t)) \tag{8}$$

where $\lambda_t$ is the thermal conductivity, $\rho$ is the density and $C_p$ is the specific heat. At the interface with the vapour phase, where the energy balance includes the energy flux from the surface into the flow space, the energy equation becomes [24]

$$q_{sf} = u(\rho_v Q_v + E + \rho_v u^2/2 + p_s). \tag{9}$$

Here $u$ is the vapour velocity, $\rho_v$ is the vapour density, $Q_v$ is the heat of evaporation and $E$ is the internal energy above the saturation temperature.

### Mass evolution from the surface

The saturated vapour pressure at the surface is estimated via classical thermodynamic relations between temperature and vapour pressure [26]:

$$p_s = p_o \exp[Q_v/(kT_b) - Q_v/(kT_s)] \tag{10}$$

where $T_b$ is the boiling temperature of the target material at the ambient pressure $p_o$, $k$ is the Boltzmann constant and $T_s$ is the target surface temperature at the melt–vapour interface. The mass flux is given by

$$J = \sqrt{m/2\pi k}\left(\Gamma \frac{\sigma_c p_v}{\sqrt{T_v}} - \frac{\sigma_e p_s}{\sqrt{T_s}}\right). \tag{11}$$

$\Gamma$ is a Maxwellian factor, $m$ is the atomic mass and the coefficients $\sigma_e$ and $\sigma_c$ are evaporation and condensation coefficients, respectively.

During the laser pulse, the rapid evaporation will result in a Knudsen layer at the surface, where translational equilibrium is not yet reached [27]. The resulting jump in parameters was not modelled in detail because the long timescale evolution of the plume is not significantly affected by this short-term near-surface effect.

## Plasma ionization, recombination and absorption of light

As the vapour pressure begins to build up, ionization can be initiated either through direct heating or by a collisional cascade of electrons in the strong electric field of the laser, i.e. laser-induced breakdown. The laser intensities utilized in our work (of the order of $10^9$ W cm$^{-2}$) are well below the breakdown threshold of most gases [28], such that ionization is assumed to be dominated by thermal effects.

We estimated the ionization state using a density-corrected Saha equation [29]:

$$\frac{n_i}{n_o} \approx 2.4 \times 10^{15} \frac{T_e^{3/2}}{n_i} \exp^{-U_i/kT_e} \qquad (12)$$

where $U_i$ is the density-corrected ionization energy, $n_i$ is the density of ionized atoms, $n_o$ is the density of neutral atoms and $T_e$ is the plasma temperature. Peak values range from 0.001 to 1.0 for laser intensities from $5 \times 10^7$ to $5 \times 10^9$ W cm$^{-2}$.

The resulting plasma in front of the surface will absorb a fraction of the incident laser light during the pulse. This absorption occurs by inverse bremsstrahlung with attenuation length $\kappa$ given by [15]

$$k = 6.52 \times 10^{-24} Z^2 \left( \frac{n_i n_e}{T_e^{7/2}} \right) \, [\text{cm}^{-1}] \qquad (13)$$

where $Z$ is the effective charge state. For the laser intensities considered here, less than 1% of the incident light is absorbed by inverse bremsstrahlung.

Recombination rates are relatively slow during the later stages of plume expansion and are modelled using a rate equation instead of assuming ionization equilibrium [15]:

$$\frac{dx}{dt} = bn \left( x_{eq}^2 - x^2 \right) \qquad (14)$$

where $x = n_e/n_o$ is the degree of ionization, $x_{eq}$ is the equilibrium ionization given by the Saha equation and $b$ is the rate constant (a function of $n$ and $T$).

## Vapour and ambient hydrodynamics

The rapidly increasing vapour pressure near the surface creates a large driving force for vapour expansion. The high temperature and density lead to pressures far exceeding the background gas pressure (of the order of 10–100 atm).

In order to solve for the ensuing plume dynamics, a set of one-dimensional two-fluid equations was used. These consist of mass conservation laws for both the vapour (subscript v) and the background gas (subscript b) and a single momentum conservation law for the mixture:

$$\frac{\partial \rho_v}{\partial t} + \frac{\partial (\rho_v u)}{\partial z} = \frac{\partial}{\partial z} \left( \rho D_{vb} \frac{\partial w_v}{\partial z} \right) - m_v I_n \qquad (15)$$

$$\frac{\partial \rho_b}{\partial t} + \frac{\partial (\rho_b u)}{\partial z} = -\frac{\partial}{\partial z} \left( \rho D_{vb} \frac{\partial w_v}{\partial z} \right) \qquad (16)$$

$$\frac{\partial \rho u}{\partial t} = -\frac{\partial (\rho u u)}{\partial z} - \frac{\partial}{\partial z} \mu \frac{\partial u}{\partial z} - \frac{\partial p}{\partial z} \qquad (17)$$

where $\rho$ is the mass density, $u$ is the velocity, $D_{vb}$ is the mass diffusivity of species v into b, $w_v$ is the vapour concentration, $I_v$ is the vapour source term accounting for evaporation and condensation and $\mu$ is the gas viscosity. As the laser ablation plume expands into a low-pressure background gas, eventually the density becomes so low that the flow is no longer in a continuum regime. Based on our experience, at or before 1 $\mu$s the Knudsen number (the ratio of particle mean free path to plume size) reaches 0.1, which is a commonly accepted value at which the mean free path is too long to justify a fluid approximation. Most of the condensation physics is completed at this point in time, such that we did not attempt to adjust the flow calculations. Other researchers (e.g. [30]) have developed hybrid models which take into account scattering and interpenetration.

For simplicity the condensate was not modelled separately in the fluid dynamic calculation. It was assumed that the condensate travels at the same velocity as the vapour/gas mixture and shares the same temperature. In addition, it was assumed that the condensate does not alter the transport properties of the vapour.

## Energy conservation in the flow space

The heat transfer and thermal response in the flow space are described by an energy conservation equation for the vapour/gas mixture. It accounts for the change in internal energy, $e$, transport and sources and sinks of energy:

$$\frac{\partial e}{\partial t} + u \frac{\partial e}{\partial z} = -\frac{\partial q}{\partial z} + \mu \left( \frac{\partial u}{\partial z} \right)^2$$
$$+ \left( \frac{\partial p}{\partial t} + u \frac{\partial p}{\partial z} \right) + Q_v I_n + q_{ib} + q_r \qquad (18)$$

where $\mu$ is the fluid viscosity. The internal energy includes the ionization energy and the sources include condensation ($Q_v I_n$), laser absorption during the pulse ($q_{ib}$) and recombination ($q_r$). An additional energy source from the liquid surface is included at the boundary, as described above.

## Homogeneous nucleation and heterogeneous growth of condensate

The homogeneous nucleation rate is evaluated using the expressions in section 1. The growth of pre-existing clusters is modelled using surface condensation rates ($J_s$) obtained from the Knudsen formula and Clausius–Clapeyron relation (equations (10) and (11) are valid for condensation as well as evaporation). Agglomeration (or break up) by cluster collisions is assumed to be small. Then the total rate of nucleation (number of vapour molecules condensed per unit volume per unit time) is given by a sum of the homogeneous creation of critical clusters and agglomeration on pre-existing clusters [23]:

$$I = 4\pi J_s \int_0^\infty F(R) R^2 \, dR + \tfrac{4}{3}\pi r^{*3} n J_h \qquad (19)$$

where $F(R)$ is the radius distribution function for particles.

393
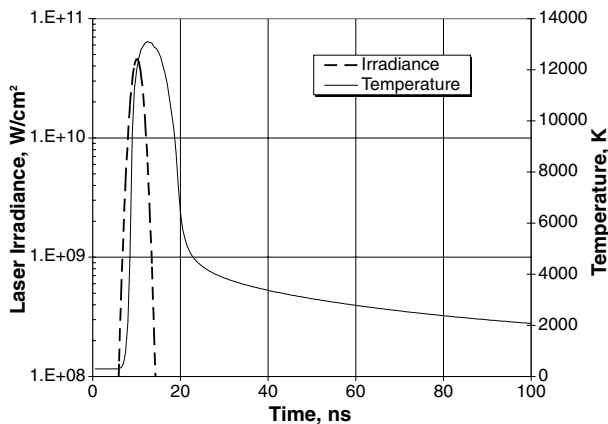
**Figure 4.** Laser irradiance and surface temperature response for the modelling test case.

In order to obtain the spatial distribution of the condensed phase numerically, the condensate distribution function is described as a system of moments, for which a series of transport equations was solved. Following Gnedovets [23], a particulate transport equation is transformed to an infinite set of moment equations by multiplying by $R^k$ and integrating over the cluster radius from zero to infinity to give a set of moment equations which relate particulate nucleation and growth rates to the condensate size distribution, taking into account cluster transport in the plasma.

*Solution methodology*

Numerically, the above set of equations was solved using an explicit Euler scheme with forward stepping in time. Spatial derivatives were approximated with simple upwind differencing to avoid oscillations in the solution, which can result in singularities in the condensation model. Each node in the domain is assumed to have constant properties for both the vapour and fluid and a single condensate number density and mean radius which is governed by the growth rate equations. A von Neumann stability analysis was performed and used to calculate appropriate time steps, which enabled stable solutions to be generated [31].

## 3. Modelling results

A representative example is described here to illustrate the main features of expansion and condensation. The target is silicon and the background gas is helium, initially at room temperature and 500 mTorr pressure. Figure 4 shows the laser intensity and surface temperature response. The incident 532 nm laser pulse is Gaussian in time with a full width at half-maximum of 5 ns and average intensity of 25 GW cm$^{-2}$. The surface temperature rises while the laser is on and then drops rapidly following the termination of the pulse. During this temperature excursion, the melting point (1420 °C) is quickly reached and the saturation pressure of Si rises rapidly, such that a violent expansion into the low-pressure background gas is initiated.

Figure 5 shows example density profiles for both the target vapour and He background gas at several times into the event.

The initial density of $\sim 10^{19}$ cm$^{-3}$ combined with a vapour temperature of 12 000 K leads to an initial pressure of the order of 15 atm. Initially, the background gas is expelled from the wall. A small amount of interpenetration occurs due to the finite diffusivity of He in Si. As the plume continues to expand, the 'contact surface' extends out further and further into the background gas. By 500 ns, rapid vapour condensation occurs both at the cooled wall and by nucleation and growth in the flow space, leading to a rapid collapse of the vapour density. At this point in time, the plume has pushed about 1.5 cm away from the wall, which is consistent with our experimental measurements (see section 4). A void region forms because the condensation occurs more rapidly than the back flux of helium. Our continuum flow model breaks down in this regime, when the plume Knudsen number exceeds 0.1, such that we terminated the model before the background gas collapsed back into the wall.

Figure 6 shows the corresponding velocity profiles. (The background gas and vapour are treated as a single fluid in the momentum equation.) After the laser pulse has terminated, the model predicts that the vapour velocity is 15 km s$^{-1}$. A peak velocity of 35 km s$^{-1}$ is achieved at about 100 ns following the pulse, as a result of the continued influx of vapour into the plume and the transfer of thermal energy into directed kinetic energy. After 100 ns, the velocity rapidly falls to values below 1 km s$^{-1}$. These values are qualitatively consistent with experimental measurements by ourselves and others, which predict peak velocities in the range of $10^4$–$10^5$ m s$^{-1}$ and initiation of drag forces (departure from free expansion) after about 100 ns [12–14].

Figure 7 depicts the temporal evolution of the ionization fraction ($n_e/n_o$) versus time in the vicinity of the target surface. The ionization state increases rapidly as the temperature rises, following the Saha equation (equation (12)). After termination of the pulse, the ionization fraction drops off more slowly than the temperature due to the rate-limited behaviour of recombination (equation (14)). A peak value of $\sim 0.02$ is reached at the end of the laser pulse.

Figure 8 shows the temporal behaviour of the saturation ratio ($p_v/p_s$) averaged over the plume for laser intensities ranging from 0.5 to 50 GW cm$^{-2}$. The spike in saturation ratio occurs much quicker for higher intensities, which is probably due to the higher vapour pressures and faster expansion rates. It also drops more quickly at higher intensities.

The peak value of saturation ratio is significantly reduced at higher laser intensities. This most likely occurs due to a combination of several effects. Condensation is reduced at elevated intensities due to the higher cluster temperature, increased heating of clusters in the plume by recombination and the high expansion velocity which rapidly creates a very low vapour pressure in the plume. The saturation ratio will decrease any time the product of the vapour density and vapour temperature falls more rapidly than the saturation pressure at the cluster surface.

Figure 9 shows the resulting average cluster size at the end of the expansion. In order to highlight the effect of ionization, cases were run with the ionization artificially set to zero. At the lowest intensity (0.05 GW cm$^{-2}$) the amount of ionization is too small to affect the particle sizes. However, for higher values the presence of ionization is predicted to significantly
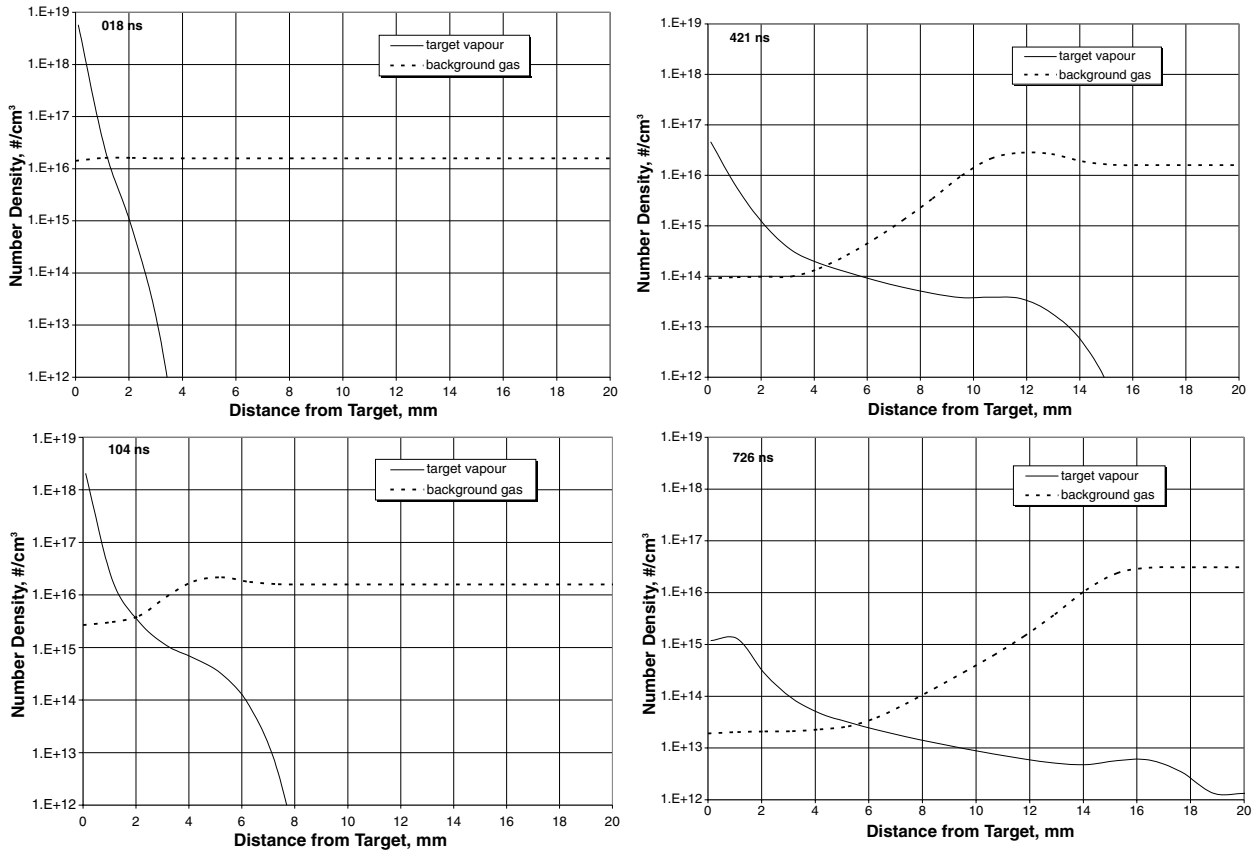
**Figure 5.** Spatial distribution of vapour density ($\rho_v$) and background gas density ($\rho_b$) at various times in the plume expansion.
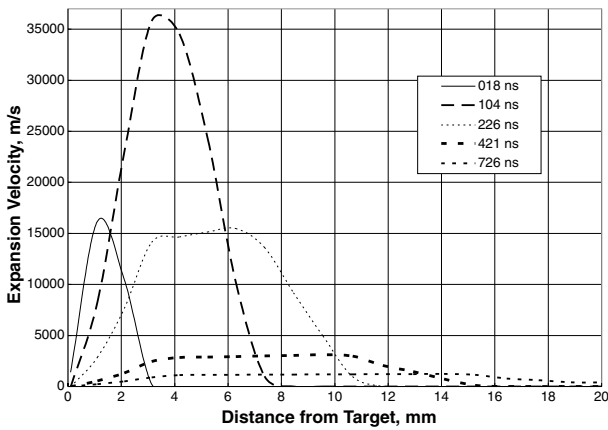


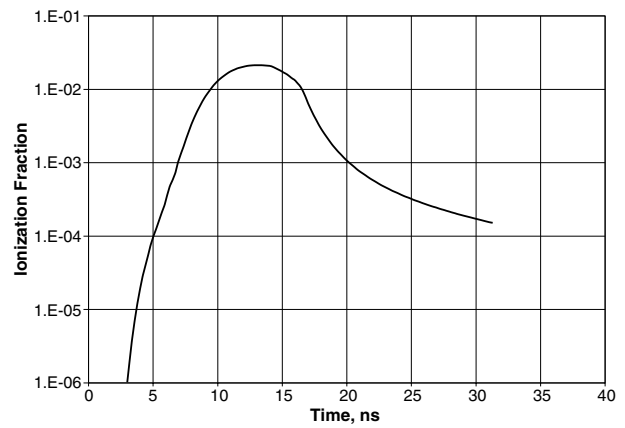**Figure 6.** Velocity profile at various times in the plume expansion for laser intensity 25 GW cm$^{-2}$.



**Figure 7.** Charge state evolution ($n_e/n$) versus time near the target surface for laser intensity 25 GW cm$^{-2}$.

decrease the particle sizes, in agreement with the predictions from section 1. As the laser intensity increases, the average particle size decreases either with or without the presence of ionization.

## 4. Experimental measurements

In this section we summarize the experimental measurements of both the plume state variables and the final size distribution of the condensate. Three primary experimental investigations were performed:

(1) A gated ICCD camera was used to image visible emission from the expanding plume.
(2) Spectroscopy was used to measure $T$ and $n$, which were then used to calculate $Z_{eff}$ and $S$. Dimer spectroscopy was also performed in order to determine the time and location at which clustering begins.
(3) Atomic force microscopy on atomic flatness witness plates was used to measure the final condensate distribution.

Figure 10 shows a schematic of the experimental set-up. Pulses from a frequency-doubled $Q$-switched Nd:YAG laser were used to create Si ablation plumes in a stainless
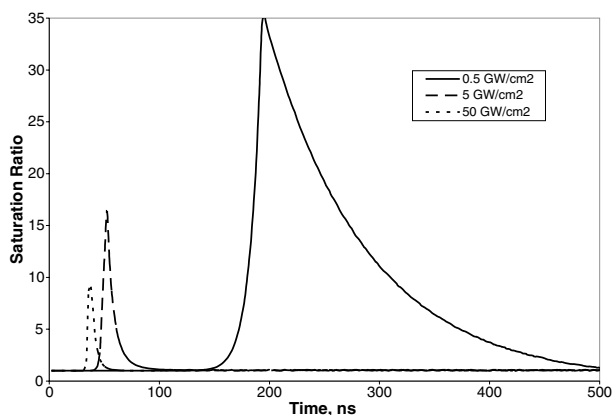
**Figure 8.** Predicted evolution of the plume-averaged saturation ratio versus time for several laser intensities.
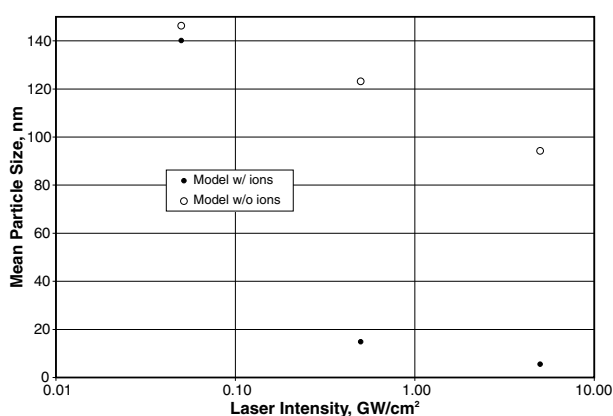


**Figure 9.** Comparison of the predicted mean particle size after 500 ns both with and without ionization considered.

steel vacuum chamber with base pressure $\sim 10^{-8}$ Torr. Injection seeding maintains a reproducible pulse with 8 ns full width at half-maximum. The laser intensity was varied by attenuating the incident pulse energy using a polarizing cube and waveplate. The spot size was kept constant for all intensities. The average laser intensity was measured using an energy meter and post-examination of the crater size. Single-crystal Si targets were rotated about an axis parallel to the beam in order to improve shot-to-shot reproducibility and to avoid drilling. Further details on the diagnostic techniques are provided in the subsections below.

### 4.1. Expansion dynamics

Imaging of the ablation plume provides an estimate of the expansion velocity as well as details on the internal structure. We utilized an intensified CCD camera (Roper PiMax model 512RB) located orthogonal to the plasma expansion direction for photographing the plume at different times after the evolution. A 2 ns gating was used to capture the images at times $<$200 ns and a wider gate (10 ns) was used for times $>$200 ns. The emission from the plasma was recorded integrally in the wavelength range 350–900 nm. In order to eliminate stray photons from the 532 nm laser light from reaching the camera, a magenta subtractive filter was used. A programmable timing generator was used to control the delay time between the

laser pulse and the imaging system with an overall temporal resolution of 1 ns.

Figure 11 shows a sequence of images collected by delaying the gate by different amounts relative to the laser pulse. Each image is captured from a single laser pulse. A movie can be constructed by adding together the images from several sequential pulses using increasing delay time. The smoothness of the plume evolution attests to the reproducibility of the data.

A position–time ($R$–$t$) plot of the position of the plume front was acquired using these images and is given in figure 12. The plume front is defined as the leading edge that exhibits 5% of the maximum emission intensity of the body of the plume. Uncertainty in the location from image to image is $\sim$10%. The plume front initially moves at $\sim 6 \times 10^6$ cm s$^{-1}$. Consistent with our earlier observations [12], the initial 50 ns appears to exhibit no slowing of the plume front and the plume front position is linear in $R$. After this brief free expansion phase, the plume front in this pressure of He is expected to follow a shock wave expansion model with $R \propto t^{0.4}$. The full line fits in figure 12 correspond to the shock model.

We used imaging data for obtaining plume lengths at different laser intensity levels. These are very helpful for positioning the witness plate used for particle characterization, as described in section 4.5.

### 4.2. Plasma temperature and density measurements

Due to theoretical uncertainties and strongly nonlinear physics, precise plume state variables (density, temperature, supersaturation and ionization fraction as a function of space and time) cannot be derived from theory in a reliable way. Therefore, these parameters which are crucial for cluster formation and growth in laser plumes were measured experimentally and related to the final measured cluster size distribution.

For space- and time-resolved spectroscopy, an optical system was used to image the plasma plume onto the entrance slit of a spectrograph, so as to have one-to-one correspondence with the sampled area of the plume and the image. The optical system was translated to monitor different parts of the plume. Spatial resolution provided by our optical system was better than 0.5 mm. The exit port of the spectrograph was coupled to an ICCD camera that was operated with vertical binning to obtain spectral intensities versus wavelength. The spectrograph is equipped with 3 gratings (150, 600 and 2400 g mm$^{-1}$).

The plasma temperature was measured using relative line intensities of silicon emission lines of the same ionization stage as described in [32] from the hot plasma in the plume. For the temperature measurement we used the ratio of line intensities of singly charged silicon ions at 358.2 and 413.1 nm. For these measurements the gate of the intensifier was set at 5 ns. Figure 13 shows the plasma temperature decay as a function of time. An initial electron temperature of about 1 eV is observed with 5 GW cm$^{-2}$ and its value falls rapidly during the first 200 ns following termination of the laser pulse, dropping to a level of 0.3–0.4 eV. Initially the plasma expands isothermally within the duration of the laser pulse and adiabatically after the termination of the pulse. During adiabatic expansion,
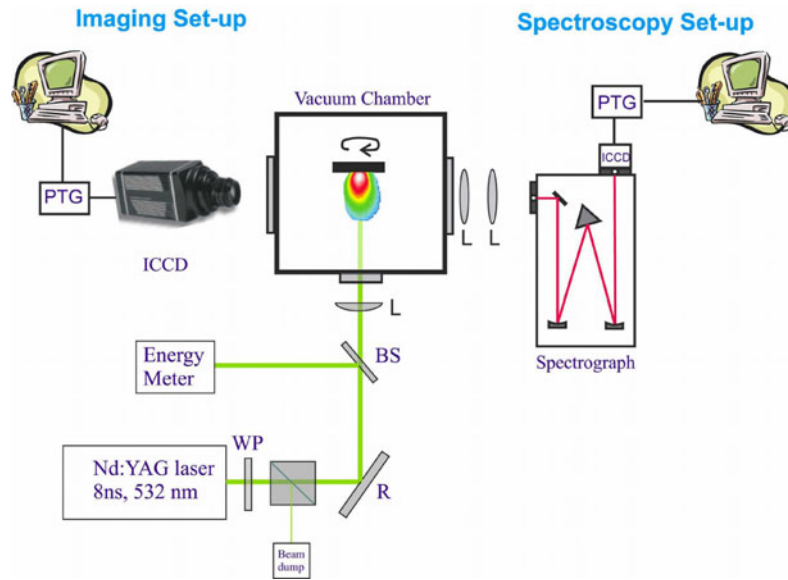
**Figure 10.** Chamber and diagnostic layout for ablation experiments (PTG, programmable timing generator; WP, wave plate; R, reflector; BS, beam sampler; L, lens).
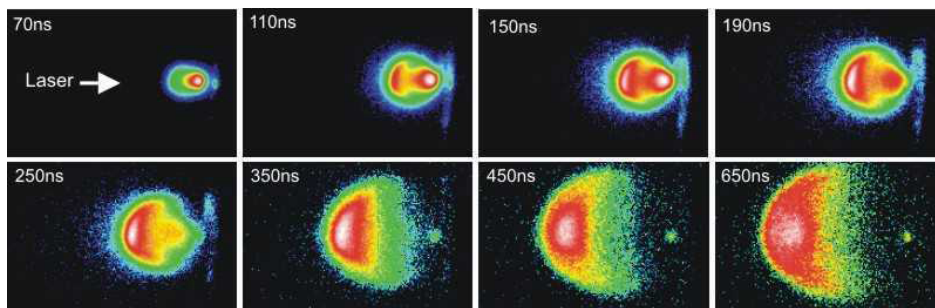


**Figure 11.** ICCD photographs of visible emission from laser-produced Si plasma at 5 GW cm$^{-2}$ average laser intensity and 500 mTorr He background gas. The timings in the images represent the time after the onset of plasma formation. All of the images are normalized to their maximum intensity. Plume behaviour indicates free expansion.

the thermal energy is converted into kinetic energy and the plasma cools down very rapidly. Measurements at times less than about 40 ns are unavailable due to the large amount of continuum radiation present. Therefore, it is difficult for us to know with certainty the plasma temperature during and immediately following the laser pulse. This information would be useful for confirming the expansion dynamics but is not needed to provide the information needed to describe the condensation physics, which begins *after* 50–100 ns (see below).
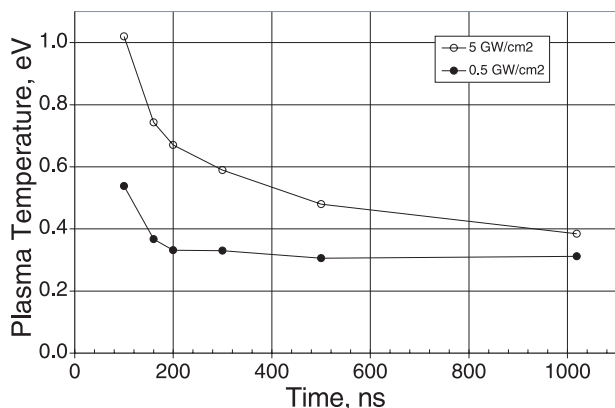
For the estimation of electron density, the Stark broadened profile of the Si–I transition at 3905 Å was measured with the monochromator at its maximum resolution. The impact parameter of this line is obtained from [33]. Besides Stark broadening, it is believed that only Doppler broadening contributes a significant amount to the total linewidth, which was found to be negligible in this experiment. Figure 14 shows the plasma density decay as a function of time. Similar to the temperature behaviour, the plasma density decreases rapidly and reaches a plateau in the range of $5 \times 10^{16}$ cm$^{-3}$. As the plume density and temperature decrease, they reach values for which recombination is very slow and heat transfer is limited by conduction.
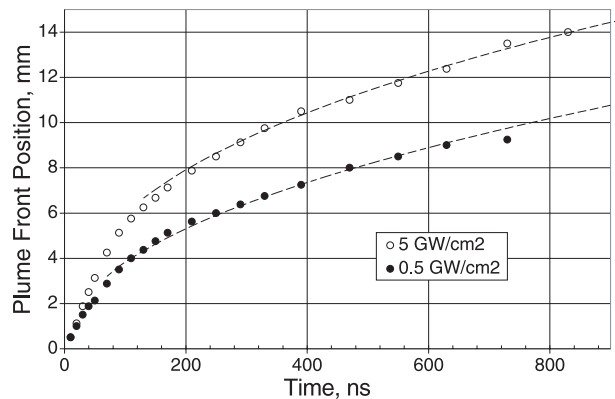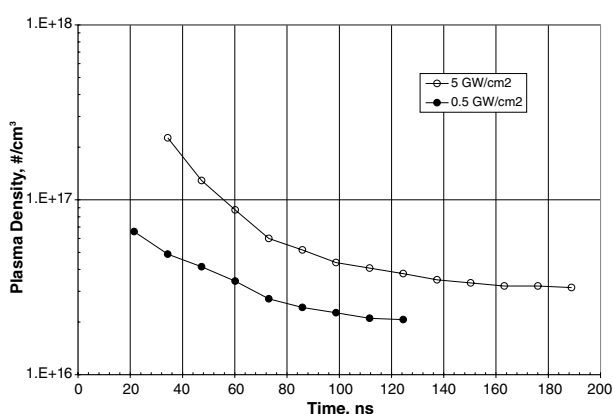


**Figure 12.** Position–time ($R$–$t$) plots of the luminous front of the Si ablation plume. The symbols in the figure represent experimental data points and the full curves represent the shock wave model ($R \propto t^{0.4}$).

### 4.3. Dimer spectroscopic results

A simple approximate measure of the onset of clustering in a plasma is the vibrational–electronic emission spectra from cluster species present in the plasma. These emissions result

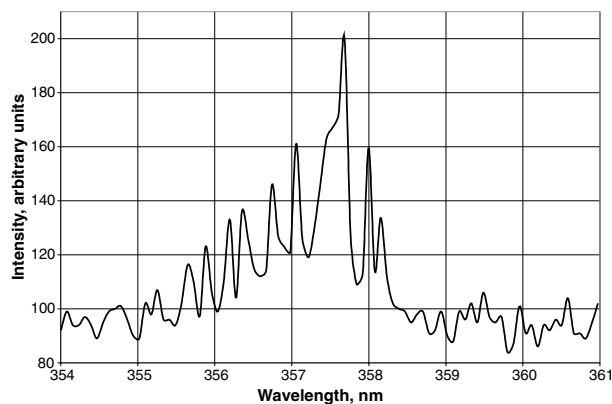**Figure 13.** Time evolution of plasma temperature at 1 mm from the target.



**Figure 15.** Typical molecular emission spectrum due to the presence of $Si_2$, taken at a distance of 10 mm from the target surface.



**Figure 14.** Time evolution of plasma density 1 mm from the target surface.



**Figure 16.** $Si^+$ and $Si_2$ vibrational emissions as a function of laser intensity and time in a 500 mTorr He background collected at a distance of 10 mm from the target surface.
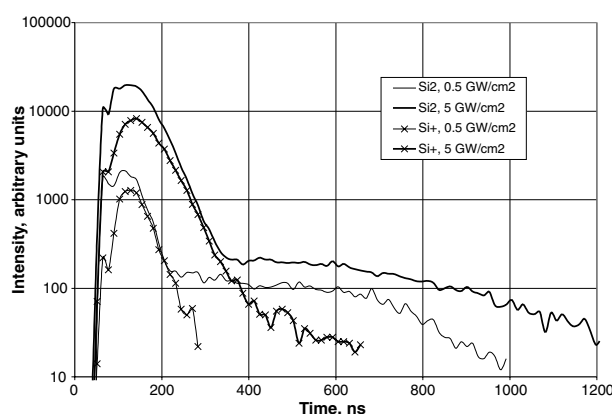
from the interaction of molecular vibrations with electronic transitions, which tend to give complex multi-line structures associated with a primary (0, 0) transition usually associated with a neutral or unperturbed molecular state. These complex spectral emissions are explained in terms of the Frank–Condon principle, which states that an electronic transition takes place so rapidly that a vibrating molecule does not change its inter-nuclear distance appreciably during any given transition. Hence, we observe many independent electronic emission lines associated with the many complex vibrational states of the molecular structure under study [34]. A typical emission spectrum of $Si_2$ observed during this experiment can be seen in figure 15.

We measured the time-resolved emission lines from different species in the laser plasma using a 5 ns gated, intensified CCD. It showed that most of the line emission from the Si plume is due to $Si^{2+}$, $Si^+$, Si and $Si_2$. The spectra indicate that a time delay exists for emission with respect to the incidence of the laser pulse. In addition, these measurements show that the emission lines from different emitting species are clearly related.

Figure 16 shows the emission intensity of $Si^+$ (385 nm) and $Si_2$ (357 nm) for several laser intensities. In these data, it is apparent that a relationship exists between the ionic emission spectra in the plumes under study and the degree of vibrational emission observed in the same plasma [35]. For the runs at

$5 \times 10^7$ W cm$^{-2}$, there is essentially no ionization signal, which remains constant barely above the thermal noise in the CCD. The runs at $5 \times 10^8$ W cm$^{-2}$ exhibit a significant signal from the $Si^+$ line at $\lambda = 412.8$ nm, which corresponds to the peak in $Si_2$ emissions observed at that intensity. The $5 \times 10^9$ W cm$^{-2}$ runs have approximately ten times that amount of emission for both $Si_2$ and $Si^+$ and the same relationship is observed.

The formation of dimers can happen from one of two situations: either the dimers are formed in the presence of ions in densities proportional to the ion density or a similar density ratio of ions to dimers leaves the target surface initially [36]. It is unlikely that a significant number of dimers is emitted from the target surface because the bond energy of $Si_2$ is only about 1 eV [37], as compared with the first ionization energy of atomic silicon of 8.1 eV. Additionally, in the highly collisional early plasma immediately adjacent to the target surface, thermal equilibration happens extremely rapidly (of the order of a picosecond).

This point is also borne out when one examines the molecular, ionic and atomic spectra as a function of distance from the target at the higher laser intensities ($5 \times 10^8$–$5 \times 10^9$ W cm$^{-2}$). We noticed at close distances most of the emission lines are due to ionic species. Any molecular emission from $Si_2$ species, if present, exists in such small amounts as to be indistinguishable from the continuum. At

this point the emitting plasma is too hot to allow the formation of clusters. Further, if clusters were emitted directly from the surface at these intensities, one would observe molecular emission at this stage.

At greater distances $Si_2$ molecular emissions appear accompanied with $Si^{2+}$, $Si^+$ and Si neutral atomic emissions. This makes sense when one considers the fact that the emitted plasma flows from the hot target into a cold background gas. In this case, one would expect to see a cooling at the leading edge of the plasma in contact with the background. This is caused by simple inter-diffusion with the cold background gas. Behind that leading edge, the plasma is cooled only through radiative emission and the work of expansion, and therefore remains hotter and would be expected to contain species at a higher average temperature and ionization state.

Some interesting information regarding the onset and duration of nucleation can also be derived through these data when one remembers that the initial expansion velocity of the plasma plume at these laser intensities was of the order of $6 \times 10^6$ cm s$^{-1}$ and there is no appreciable emission at the 2 mm location until about 50 ns and at that point in time, as previously described, there is no molecular emission noted. At the 6 mm location, which takes the plume about 100 ns to reach, there are consistently distinct molecular emissions noted in the data. Overall, this means that the dimer emission probably begins in earnest sometime between approximately 50 and 100 ns.

Additionally, the duration of molecular emission provides some insight into the duration of cluster nucleation in the plasma. At 6 and 10 mm, the duration of molecular emission lasts about 400 and 800 ns, respectively. That suggests the duration of the cluster birth phase in the plasma at these conditions is somewhere between 400 and 800 ns. As previously mentioned, one would expect this birth phase to be followed by a phase which is dominated by heterogeneous cluster growth.

Overall, a number of conclusions can be drawn from these data. First, it is unlikely that dimers are emitted from the surface of the target, since molecular spectra are not observed near the target at any time. Second, ionic and molecular emission are seen to be coincident at distances further from the surface of the target, which indicates that ions are present at the same time as clusters are initially formed. Finally, clustering in the plasma begins sometime between 40 and 100 ns and substantially decreases in about a microsecond, suggesting the bulk of cluster births occurs relatively early in the expansion.

### 4.4. Ionization and supersaturation

Spectroscopic measurements of plasma density and temperature allow us to approximate the saturation ratio and effective charge state. In order to proceed, we assumed local thermodynamic equilibrium (LTE). This was justified *a posteriori* by satisfying the McWhirter criterion using the measured values of $n_e$ and $T_e$ [32]. Given an electron density and temperature, the neutral density was calculated using the Saha equation. The average charge state is given simply by $n_e/n_o$ (i.e. the maximum possible charge state for Si would be 14). In order to supplement our data at 0.5 and 5 GW cm$^{-2}$, we also derived and present the saturation ratio and ionization fraction at 50 GW cm$^{-2}$ using data from [38]. Those data were
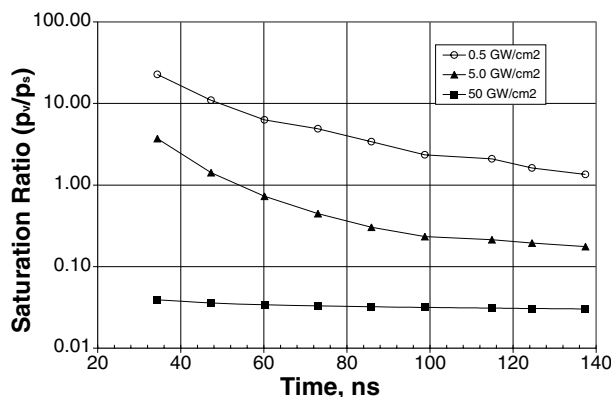


**Figure 17.** Saturation ratio at 1 mm from the target, derived from spectroscopy and assuming local thermodynamic equilibrium (data at 50 GW cm$^{-2}$ from [38]).
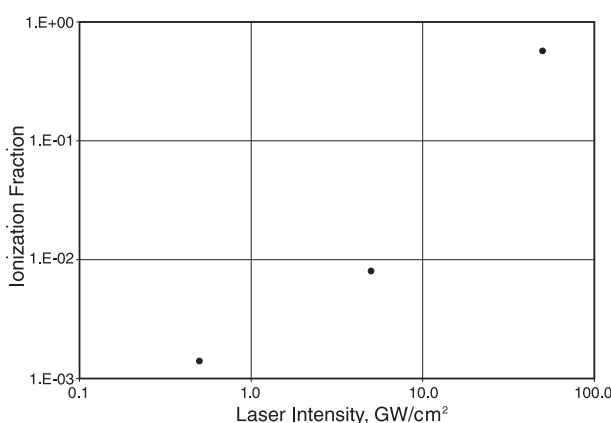


**Figure 18.** Maximum charge state at 50 ns, 1 mm from the target, as derived from spectroscopy and assuming local thermodynamic equilibrium (data at 50 GW cm$^{-2}$ from [38]).

obtained using carbon expanding into vacuum; however, the atomic number is sufficiently close that the trends appear to be consistent.

Figure 17 shows the resulting saturation ratio at $x = 1$ mm. Somewhat surprisingly, the saturation ratio *decreases* as the laser intensity *increases*. Figure 18 shows the maximum charge state of the plasma as a function of laser intensity. The supersaturation data indicate an inverse relationship with increasing ionization fraction. Since supersaturation is the main variable upon which the condensation rate is dependent, that must be interpreted as a change in mechanism taking place with increasing ionization in the plasma: from homogeneous to heterogeneous condensation upon ions. Homogeneous condensation occurs at relatively large levels of supersaturation since, energetically speaking, it is a higher energy condensation pathway. Conversely, heterogeneous condensation is not associated with high levels of supersaturation as vapour atoms simply condense upon existing surfaces provided by the cluster-ion seedlings.

The saturation ratio in the plume is lower at higher laser intensities. In fact, at 50 GW cm$^{-2}$ the plume is sub-saturated at all times that we could measure (i.e. the clusters should experience evaporation under these conditions). At reduced saturation ratio, one would expect the ion seed pathway to become more important; however, as the intensity continues to

increase, eventually condensation will stop due to high cluster temperature, heating by recombination and the high expansion velocity which creates a very low vapour pressure in the plume. Modelling results predict an early spike in the saturation ratio even for this intensity (figure 7), but our experimental data are limited to times greater than about 40 ns. It seems highly likely that condensation processes existed in the earliest stages of the plume expansion, since we measured a significant number of clusters on witness plates. These observations also agree with research results in the field of thin film deposition by PLD, where decreased condensate deposition is obtained using higher laser intensities [39].
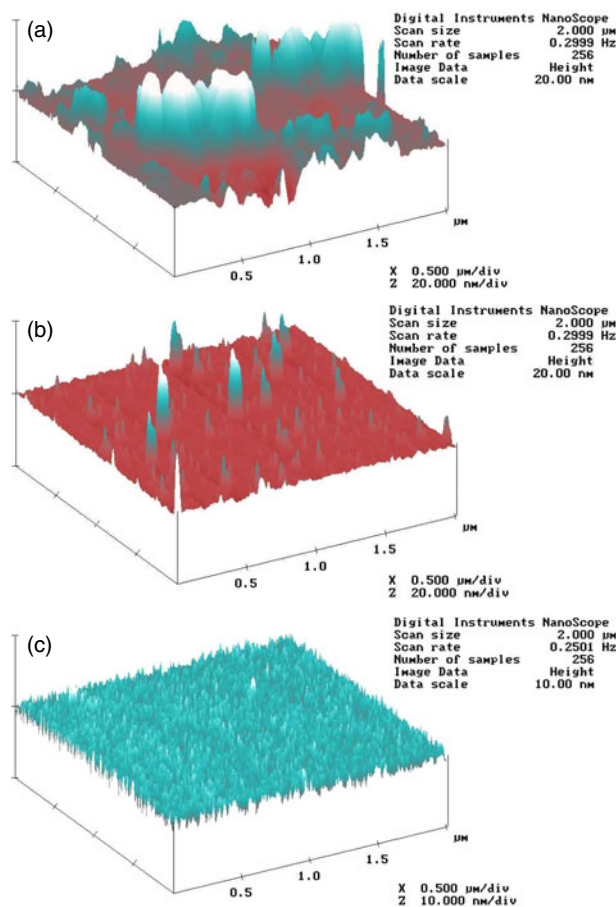
### 4.5. Final cluster size distribution

Nanoparticle diagnostics represent an active area of research and many methods have been used to attempt to measure the particulate size distribution of a sample of aerosol. These include use of a witness plate, differential mobility analyser, laser-induced incandescence, light scattering techniques, etc [21, 40–43]. Witness plate methods coupled with atomic force microscopy offer advantages over other methods in that they are relatively easily calibrated, offer reliable volume information and experimental simplicity enabling, in the present work, plasma state data to be easily taken simultaneously. Volume information is important because particulate morphology may not remain spherical, especially when clusters are collected *in situ* at high velocity. In addition, when using witness plates one does not need to assume a predetermined size range for analysis as with other methods. The major downside associated with this approach is the need to fabricate atomic flatness witness plates in order to make reliable measurements. These plates must be carefully fabricated and handled to ensure their flatness and cleanliness.

Cluster size distributions were measured using atomic force microscopy (AFM) on witness plates which were fabricated with near-atomic flatness. Witness plates were prepared starting with single-crystal Si wafers. In order to achieve the flattest possible surface, the native oxide was stripped with HF and then, after cleaning, a controlled thermal oxide was grown at a temperature of 1350 K up to about 1 $\mu$m thickness. The resulting surface has a roughness of $\sim$4 Å, which was verified using AFM. The final step was to apply a metallic sputter coating of Au or Ta in order to allow us to perform scanning electron microscopy (SEM) on the surface.

The witness plates were placed in the path of the expanding plumes at a distance close to the stagnation point predicted from our plume imaging results, which depends on the laser intensity. At low background pressures, the plume does not come to a complete stop. However, the process of condensation is nearly complete after 500–1000 ns, such that the small residual velocity in the late stage of plume expansion is not expected to alter the final cluster size distribution. In fact, a small residual velocity is needed in order to transport the clusters to the witness plate.

This use of witness plates, while far easier than *in situ* diagnostics (based on light scattering, for example), limits us to measuring only the final size distribution that reaches the plate. For all experiments, a control specimen was transported together with the test specimen throughout all stages of testing in order to verify the absence of contamination. Inside the test
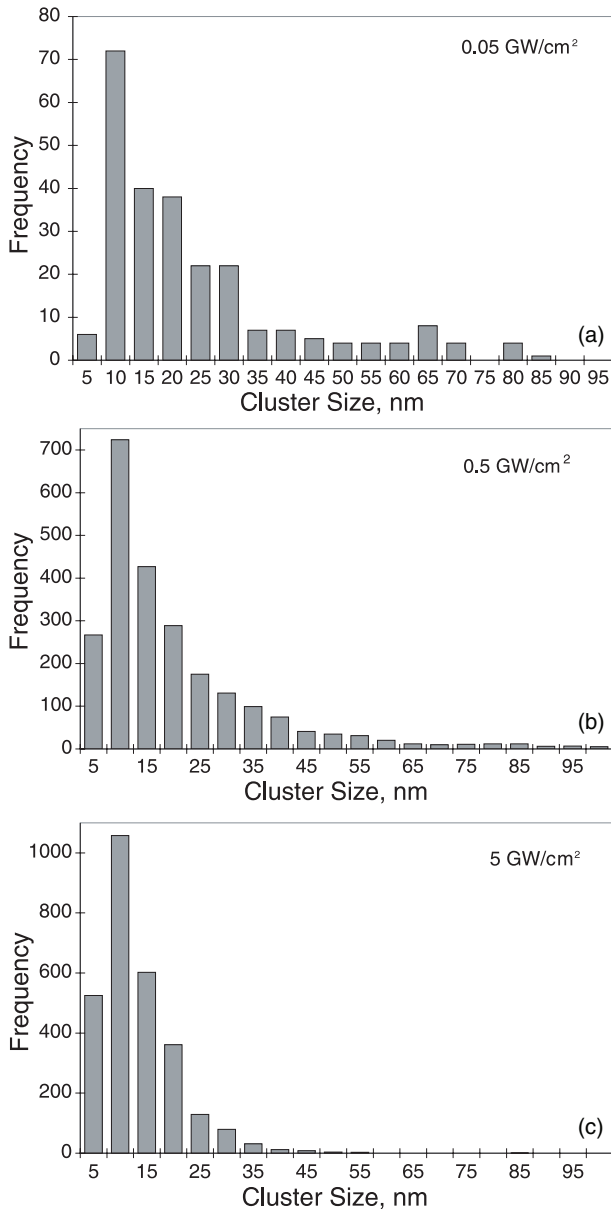


**Figure 19.** AFM measurement of cluster size distribution on witness plates for several laser intensities: (a) $5 \times 10^7$ W cm$^{-2}$, (b) $5 \times 10^8$ W cm$^{-2}$ and (c) $5 \times 10^9$ W cm$^{-2}$. In all cases the background He pressure was 500 mTorr.

chamber the control specimen was masked to avoid coating with ablation products.

Figure 19 shows example results of AFM on specimens exposed to an average intensity of $5 \times 10^8$ and $5 \times 10^9$ W cm$^{-2}$, respectively. All the experiments were performed at a helium pressure of 500 mTorr. Already from these nanographs one can see evidence of the decrease in mean particle size with increasing laser intensity. Figure 20 shows histograms of the particle size distribution measured with AFM for three intensity levels, from $5 \times 10^7$ to $5 \times 10^9$ W cm$^{-2}$. The histograms indicate that a relatively small decrease in mean particle size occurs in the lower intensity regime, but a fairly marked decrease occurs when the intensity increases from $5 \times 10^8$ to $5 \times 10^9$ W cm$^{-2}$. Here the mean is defined as the arithmetic mean radius of clusters. Since larger clusters contain more mass, the amount of condensate tied up in larger clusters increases more rapidly than the mean radius.

AFM was performed in tapping mode using a Digital Instruments D5000 with a 5 nm radius tapping-mode etched silicon probe (TESP). The nominal resolution of the height measurement is $\sim$1 Å. However, additional uncertainties arise in the data when clusters are not clearly separated in a single monolayer.

Figure 21 summarizes the trend in average particle size with increasing laser intensity. The modelling result represents

**Figure 20.** Cluster size histogram at several laser intensities: (a) $5 \times 10^7$ W cm$^{-2}$, (b) $5 \times 10^8$ W cm$^{-2}$ and (c) $5 \times 10^9$ W cm$^{-2}$.

the mean size predicted after all condensation processes are completed, whereas the experimental data were acquired at a location which we predicted would capture particles in their final state.

In our work, the particle size distribution is found to decrease with increasing laser irradiance. Recently, Patrone *et al* [44] observed that mean cluster size is a growing function of laser fluence during ArF laser ablation of a Si target at 4 Torr helium background pressure. They used the target itself as the witness plate and performed the experiments in a small intensity range ($0.67$–$2.6 \times 10^8$ W cm$^{-2}$) compared to the present experiments. Moreover, the high background pressure used in their experiment supported the enhanced backflow of the species towards the target. In contrast, Seto *et al* [45] observed that the size of the nanoparticles generated by Si ablation using radiation from a frequency-doubled $Q$-switched Nd:YAG laser decreases with increasing power density, which
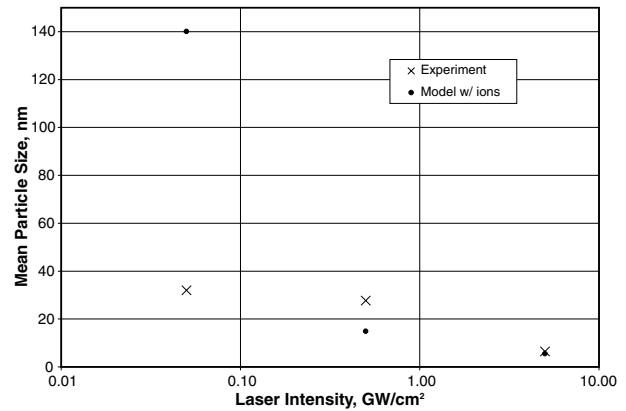


**Figure 21.** Comparison of experiments and modelling of mean cluster size versus laser intensity.

is in agreement with the present experimental results. Their experimental conditions are similar to those used in the present studies, except for the background pressure (5 Torr helium) and laser intensity range used (2–8 GW cm$^{-2}$). This indicates that the size and spatial distribution of nanoclusters within the laser created plume are determined by the hydrodynamics of expansion and strongly depend upon the initial conditions, laser irradiance and pressure of the background gas [46].

As can be seen in figure 21, the computational model diverges at the lower laser intensities. This may be due to the fact that, in actuality, there are a significant number of electrons present even at the lowest laser intensity level, which influence the nucleation processes in the plasma and decrease the average particle size. Since the model does not effectively represent these low levels of ionization, these electrons are not taken into account in the birth phase of the condensation process. Hence the predicted particle size may be significantly inaccurate.

## 5. Summary and conclusions

The influence of ionization on cluster formation in laser plasma was investigated experimentally and numerically. Ionization has been shown to be present in virtually all laser ablation plumes, even those only slightly above the ablation threshold. Due to the strong dependence, the condensation of virtually any practical laser plume takes place under the influence of ionization. Although no single piece of data provides decisive proof, all the evidence suggests that ionization plays a dominant role in the formation of clusters in laser ablation plumes. This evidence comes from fundamental theory, numerical modelling and experimental measurements of the plume evolution and final condensate distribution.

Fundamental theory suggests that ions depress the formation energy of clusters due to dielectric attraction to surrounding vapour atoms, which increases the homogeneous nucleation rate by orders of magnitude. This leads to a larger number of seed sites during the cluster creation phase of the plume expansion and, consequently, a smaller average cluster size after all of the vapour has condensed.

Numerical modelling of the temporal and spatial characteristics of the rapidly evolving ablation plume agrees with this first-principles prediction. Our modelling work

showed qualitative agreement in most cases with our experimental results. This agreement is facilitated by the fact that the target absorption depth and plasma recombination coefficient were derived via experiment. However, the nonlinearity of the physics associated with the formation of laser plasma and condensation makes this an extremely difficult and numerically unstable modelling task.

Due to our limited ability to model the complex nonlinear processes in a laser ablation plume, experiments were used to isolate and discern quantitative information on all variables related to cluster formation for one set of experimental conditions. In these experiments, laser intensity was employed as a means of varying the plasma ionization state. The data include plume state variables, dimer and ion spectroscopy and witness plate measurements of the final cluster size distribution.

Plasma spectroscopy was used to measure the plasma temperature and density, from which the degree of plume ionization and saturation ratio were derived. These measurements showed that the saturation ratio decreased with increasing laser intensity, whereas the charge state increased. At reduced saturation ratio, the ion seed pathway becomes more important. However, eventually condensation will stop due to the high cluster temperature, heating by recombination and the high expansion velocity which creates a very low vapour pressure in the plume. The amount of data available is not sufficient to provide a comprehensive treatment of the temporal and spatial evolution of the plume. Additional work is needed in order to pinpoint the time and location where condensation occurs and to provide more thorough benchmarking of model predictions

Spectroscopic investigation of the temporal and spatial variations of various species in the laser plasma suggest a correlation between the ionic, neutral and molecular spectral emissions emanating from the plasma. This understanding gives a strong indication that the presence of ions is accompanied by nascent clusters in the form of $Si_2$, which strengthens the relationship between clusters and ions in both space and time. Questions still remain as to the exact nature of this coupling, which should be the subject of future investigations.

Silicon nanoclusters were captured on nanometre-scale flat silicon witness plates by laser ablation of a (100) Si target. Witness plate substrates were read with an atomic force microscope to investigate the final cluster distributions, which were then correlated with the plasma state parameters. The witness plate measurements clearly indicated an increase in the number density and decrease in average size of the clusters formed as the laser intensity increased. This agrees with the observation that ions increase the homogeneous nucleation rate, which leads to a larger number of smaller particles in the final condensate distribution.

Upon careful examination and integration of all the data collected throughout this work, a model describing cluster formation, in which ions play an important role, begins to emerge. First, the number of clusters formed is well correlated to the number of ions present in the system, which is precisely what one would expect if ions play a role in the condensation process. Second, the average cluster size decreases with increasing ionization fraction, which

also makes sense if roughly the same amount of vapour is to be condensed onto a larger number of ion clusters. Third, the supersaturation data indicate an inverse relationship with increasing ionization fraction. Since supersaturation is the main variable upon which the condensation rate is dependent, that must be interpreted as a change in the mechanism taking place with increasing ionization in the plasma: from homogeneous to heterogeneous condensation upon ions. Homogeneous condensation occurs at relatively large levels of supersaturation since, energetically speaking, it is a higher energy condensation pathway. Conversely, heterogeneous condensation is not associated with high levels of supersaturation because vapour atoms simply condense upon existing surfaces provided by the cluster-ion seedlings. Overall, a preponderance of the evidence suggests that the presence of ions is central to the formation of clusters in laser plasma.

## References

[1] Chrisey D B and Hubler G K (ed) 1994 *Pulsed Laser Deposition of Thin films* (New York: Wiley)

[2] Geohegan D B, Puretzky A A, Duscher G and Pennycook S J 1998 Time-resolved imaging of gas phase nanoparticle synthesis by laser ablation *Appl. Phys. Lett.* **72** 2987–9

[3] Kroto H W, Heath J R, O'Brien S C, Curl R F and Smalley R E 1985 C60 Buckminsterfullerene *Nature* **318** 162–3

[4] Becker M, Brock J, Cai H, Henneke D, Keto J, Lee J, Nichols W and Glicksman H 1998 Metal nanoparticles generated by laser ablation *Nanostruct. Mater.* **10** 853–63

[5] Von Allmen M 1987 *Laser–Beam Interactions With Materials: Physical Principles and Applications* (Berlin: Springer)

[6] Harilal S S, Bindhu C V, Nampoori V P N and Vallabhan C P G 1998 Influence of ambient gas on the temperature and density of laser produced carbon plasma *Appl. Phys. Lett.* **72** 167–9

[7] Harilal S S 2001 Expansion dynamics of laser ablated carbon plasma plume in helium ambient *Appl. Surf. Sci.* **172** 103–9

[8] Geohegan D B 1994 *Pulsed Laser Deposition of Thin Films* ed D B Chrisey and G K Hubler (New York: Wiley) pp 115–65

[9] Geohegan D B and Puretzky A A 1995 Dynamics of laser ablation plume penetration through low pressure background gases *Appl. Phys. Lett.* **67** 197–9

[10] Bulgakov A V and Bulgakova N M 1995 Dynamics of laser-induced plume expansion into an ambient gas during film deposition *J. Phys. D: Appl. Phys.* **28** 1710–8

[11] Bulgakov A V and Bulgakova N M 1998 Gas-dynamic effects of the interaction between a pulsed laser-ablation plume and the ambient gas: analogy with an underexpanded jet *J. Phys. D: Appl. Phys.* **31** 693–703

[12] Harilal S S, Bindhu C V, Tillack M S, Najmabadi F and Gaeris A C 2003 Internal structure and expansion dynamics of laser ablation plumes into ambient gases *J. Appl. Phys.* **93** 2380–8

[13] Rai V N, Shukla M and Pant H C 2000 Effect of chamber pressure induced space charge potential on ion acceleration in laser produced plasma *Laser Part. Beams* **18** 315–24

[14] Chen K R, Leboeuf J N, Wood R F, Geohegan D B, Donato J M, Liu C L and Puretzky A A 1995 Accelerated expansion of laser-ablated materials near a solid surface *Phys. Rev. Lett.* **75** 4706–9

[15] Zeldovich Y and Raizer Y 1967 *Physics of Shock Waves and High-Temperature Hydrodynamic Phenomena* (New York: Academic)

[16] Kashchiev D 2000 *Nucleation: Basic Theory with Applications* (Oxford: Butterworth Heinemann)

[17] Zettlemoyer A C (ed) 1969 *Nucleation* (New York: Dekker)
[18] Russell K 1969 Nucleation on gaseous ions *J. Chem. Phys.* **5** 1809–16
[19] Toftmann B, Schou J, Hansen T N and Lunney J G 2000 Angular distribution of electron temperature and density in a laser-ablation plume *Phys. Rev. Lett.* **84** 3998–4001
[20] Mayo R M, Newman J W, Sharma A, Yamagata Y and Narayan J 1999 Electrostatic measurement of plasma plume characteristics in pulsed laser evaporated carbon *J. Appl. Phys.* **86** 2865–71
[21] Tosto S 1999 Modeling and computer simulation of pulsed-laser-induced ablation *Appl. Phys.* A **68** 439–46
[22] Leboeuf J N, Chen K R, Donato J M, Geohegan D B, Liu C L, Puretzky A A and Wood R F 1996 Modeling of plume dynamics in laser ablation processes for thin film deposition of materials *Phys. Plasmas* **3** 2203–9
[23] Gnedovets A, Gusarov A and Smurov I 1999 A model for nanoparticles synthesis by pulsed laser evaporation *J. Phys. D: Appl. Phys.* **32** 2162–8
[24] Gusarov A, Gnedovets A and Smurov I 2000 Two-dimensional gas-dynamic model of laser ablation in an ambient gas *Appl. Surf. Sci.* **154/155** 66–72
[25] Le H C, Zeitoun D E, Parisse J D, Sentis M and Marine W 2000 Modeling of gas dynamics for a laser-generated plasma: propagation into low-pressure gases *Phys. Rev.* E **62** 4152–61
[26] Collier J G 1981 *Convective Boiling and Condensation* 2nd edn (New York: McGraw-Hill)
[27] Knight C J 1979 Theoretical modeling of rapid surface vaporization with back pressure *AIAA J.* **17** 519–23
[28] Turcu I C E, Gower M C and Huntington P 1997 Measurement of KrF laser breakdown threshold in gases *Opt. Commun.* **134** 66–8
[29] Griem R H 1962 High density corrections in plasma spectroscopy *Phys. Rev.* **128** 997–1003
[30] Wood R F, Leboeuf J N, Geohegan D B, Puretzky A A and Chen K R 1998 Dynamics of plume propagation and splitting during pulsed-laser ablation of Si in He and Ar *Phys. Rev.* B **58** 1533–43
[31] Ferziger J and Peric M 1996 *Computational Methods for Fluid Dynamics* (Berlin: Springer)
[32] Griem H R 1997 *Principles of Plasma Spectroscopy* (New York: Cambridge University Press)
[33] Griem H R 1964 *Plasma Spectroscopy* (New York: McGraw-Hill)
[34] Banwell C 1972 *Fundamentals of Molecular Spectroscopy* (London: McGraw-Hill)
[35] Douglas A 1955 The spectrum of $Si_2$ molecule *Can. J. Phys.* **33** 801–5
[36] Harilal S S, Issac R C, Bindhu C V, Nampoori V P N and Vallabhan C P G 1996 Temporal and spatial evolution of Ca in laser induced plasma from graphite target *J. Appl. Phys.* **80** 3561–5
[37] Redondo A, Goddard W A and McGill T C 1982 Mott insulator model of the Si(111)-(2 × 1) surface *J. Vac. Sci. Technol.* **21** 649–54
[38] Harilal S S, Bindhu C V, Issac R C, Nampoori V P N and Vallabhan C P G 1997 Electron density and temperature measurements in a laser produced carbon plasma *J. Appl. Phys.* **82** 2140–6
[39] Riedo E, Comin F, Chevrier J, Schmithusen F, Decossas S and Sancrotti M 2000 Structural properties and surface morphology of laser-deposited amorphous carbon and carbon nitride films *Surf. Coat. Technol.* **125** 124–8
[40] Will S, Schraml S, Bader K and Leipertz A 1998 Performance characteristics of soot primary particle size measurements by time-resolved laser-induced incandescence *Appl. Opt.* **37** 5647–58
[41] Geohegan D B, Puretzky A A, Duscher G and Pennycook S J 1998 Photoluminescence from gas-suspended $SiO_x$ nanoparticles synthesized by laser ablation *Appl. Phys. Lett.* **73** 438–40
[42] Landstrom L, Marton Z, Arnold N, Hogberg H, Boman M and Heszler P 2003 *In situ* monitoring of size distributions and characterization of nanoparticles during W ablation in nitrogen atmosphere *J. Appl. Phys.* **94** 2011–8
[43] Jones A R 1999 Light scattering for particle characterization *Prog. Energy Combust. Sci.* **25** 1–53
[44] Patrone L, Nelson D, Safarov V I, Sentis M, Marine W and Giorgio S 2000 Photoluminescence of silicon nanoclusters with reduced size dispersion produced by laser ablation *J. Appl. Phys.* **87** 3829–37
[45] Seto T, Kawakami Y, Suzuki N, Hirasawa M, Kano S, Aya N, Sasaki S and Shimura H 2001 Evaluation of morphology and size distribution of silicon and titanium oxide nanoparticles generated by laser ablation *J. Nanoparticle Res.* **3** 185–91
[46] Luk'yanchuk B S, Marine W and Anisimov S I 1998 Condensation of vapor and nanoclusters formation within the vapor plume, produced by ns-laser ablation of Si *Laser Phys.* **8** 291–302